

Separating Altermagnetic and Ferromagnetic Effects in X-ray Magnetic Dichroism of Rutile NiF_2

A. Hariki,^{1,*} K. Sakurai,^{1,*} T. Okauchi,¹ and J. Kuneš²

¹*Department of Physics and Electronics, Graduate School of Engineering, Osaka Metropolitan University, 1-1 Gakuen-cho, Nakaku, Sakai, Osaka 599-8531, Japan[†]*

²*Department of Condensed Matter Physics, Faculty of Science, Masaryk University, Kotlářská 2, 611 37 Brno, Czechia[‡]*

We present numerical simulations of x-ray magnetic circular dichroism (XMCD) at the $L_{2,3}$ edge of Ni in the weakly ferromagnetic altermagnet NiF_2 . Our results predict a significant XMCD signal for light propagating perpendicular to the magnetic moments, which are approximately aligned along the [100] easy-axis direction. The analysis shows that the altermagnetic and ferromagnetic contributions to the XMCD signal can be uniquely distinguished by their dependence on an applied magnetic field. By varying the angle of the field relative to the easy axis, the in-plane orientation of both the Néel vector and the net magnetization can be systematically controlled. We further demonstrate that the XMCD signal, even under fields as strong as 40 T and for any in-plane orientation, can be accurately described as a linear combination of two spectral components, with geometrical prefactors determined by the field's magnitude and direction. This insight enables experimental validation of the distinctive relationship between the Néel vector orientation and the x-ray Hall vector in the rutile structure. Quantitative simulations supporting these findings are provided.

I. INTRODUCTION

The identification of altermagnets [1, 2] marks the emergence of a new class of collinear magnets, which, despite having no net magnetization, enable the existence of spin-polarized bands [1–12], anomalous Hall effect [6, 10, 13–18], odd magneto-optical effects [15, 19–21], and various other phenomena [22] characterized by odd Néel vector dependence.

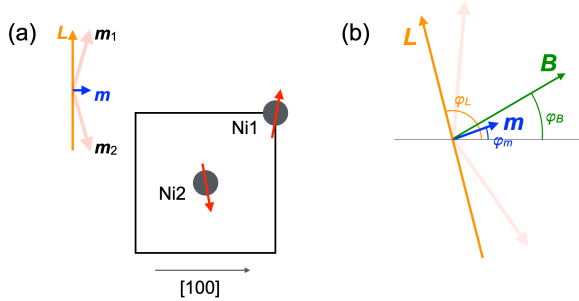


FIG. 1. (a) Top view of the rutile structure with the Néel vector \mathbf{L} in the [010] direction. The red arrows mark the local moments $\mathbf{m}_{1,2}$ in the Ni sites, \mathbf{m} is the net magnetization. (b) The definitions of angles φ_B , φ_L and φ_m measured from [100] direction where \mathbf{B} is the magnetic field applied in the (001) plane. Note that the competition between the magneto-crystalline anisotropy and the external field leads to misalignment of net magnetization \mathbf{m} and the external magnetic field \mathbf{B} .

Distinguished from conventional collinear magnets such as ferromagnets and antiferromagnets by non-relativistic symmetry operations, the characterization of altermagnets is rooted in separation between electron spin and its orbital motion. In real-world materials, however, relativistic effects such as spin-orbit coupling (SOC) invariably come into play. While typically considered a perturbation to non-relativistic symmetry, SOC becomes a critical factor for the observation of altermagnetic phenomena in some experiments [23]. Indeed, the influence of SOC is twofold: on one hand, it is indispensable for manifesting altermagnetic effects in optical and transport properties, enabling phenomena such as anomalous Hall currents or linear magneto-optical effects. On the other hand, the presence of SOC leads to competing effects, such as weak ferromagnetism, which can obscure or even mimic altermagnetic responses. This duality poses a key challenge in disentangling these intertwined behaviors experimentally. To address this challenge, x-ray spectroscopy has emerged as a powerful probe for isolating intrinsic altermagnetic effects from those induced or modified by SOC. While SOC is a prerequisite for observing magnetic dichroism, the x-ray magnetic circular dichroism (XMCD) technique leverages the large spin-orbit splitting inherent to core states, which is fundamentally distinct from weak ferromagnetism or other valence band effects. Computational studies indicate that the contribution of valence SOC to XMCD spectra is generally minor in many compounds containing 3d elements [20, 25].

In this Article we demonstrate this point in computational study of the XMCD on the Ni $L_{2,3}$ edge in NiF_2 . NiF_2 , like other members of the transition metal difluoride series, crystallizes in rutile structure and antiferromagnetically orders below 73.2 K [26]. Unlike other compounds in the series with the [001] easy axis, the Néel

* A.H. and K.S. contributed equally to this work.

[†] hariki@omu.ac.jp

[‡] kunes@physics.muni.cz

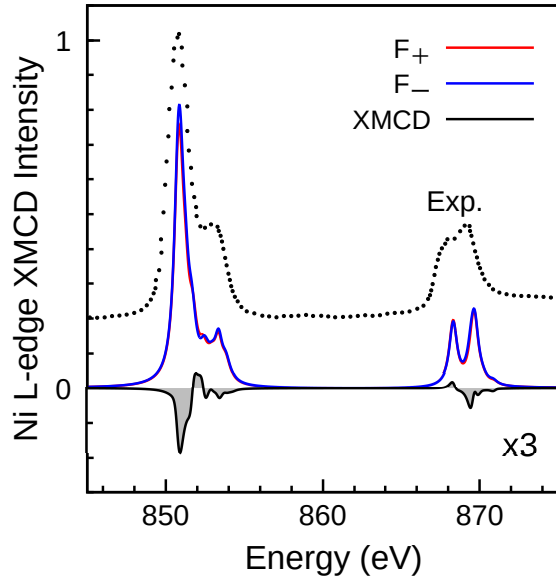


FIG. 2. The XAS calculated for the two circular polarizations (red and blue) at the Ni $L_{2,3}$ edge together with the XMCD intensities (shaded). The calculated spectral intensities are broadened by a Lorentzian of 0.30 eV (HWHM). The experimental Ni $L_{2,3}$ -edge XAS spectrum taken from Ref. 24 is shown for comparison. The experimental baseline was offset for the sake of clarity.

vector $\mathbf{L} = \mathbf{m}_1 - \mathbf{m}_2$ points along [010] or the other three direction related by the tetragonal symmetry [27, 28]. This orientation of \mathbf{L} in the rutile structure allows for a finite XMCD [19] even without an external magnetic field, assuming a single-domain sample. The valence SOC causes a small canting of the Ni moments, which results in a net magnetization along [100] and gives rise to conventional ferromagnetic XMCD signal.

The XMCD spectra for light propagating in the direction $\hat{\mathbf{k}}$ is obtained as $F_{\text{XMCD}}(\omega) = 2\mathbf{h}(\omega) \cdot \hat{\mathbf{k}}$, where the frequency dependent Hall vector $\mathbf{h}(\omega) = \text{Im}(\sigma_{zy}^a(\omega), \sigma_{xz}^a(\omega), \sigma_{yx}^a(\omega))$ depends on the orientation of the magnetic moments in the sample. Applying magnetic field \mathbf{B} in the (001) plane one can vary the moments canting as well as the orientation of the Néel vector \mathbf{L} within the (001) plane. We simulate such an experimental set-up and show that $\mathbf{h}(\omega)$ can be to a high accuracy described by two spectral functions $\Delta_{\text{ALT}}(\omega)$ and $\Delta_{\text{FM}}(\omega)$

$$\mathbf{h}(\omega) = \Delta_{\text{ALT}}(\omega)\mathcal{M}_{(110)}\hat{\mathbf{L}}(\mathbf{B}) + \Delta_{\text{FM}}(\omega)\mathbf{m}(\mathbf{B}). \quad (1)$$

Here, $\hat{\mathbf{L}}$ is the unit vector in the direction of \mathbf{L} , \mathbf{m} is the net magnetic moment per atom and $\mathcal{M}_{(110)}$ is the operation of mirror symmetry by the (110) plane. The first term is exact for a collinear antiferromagnet with rutile structure, assuming no valence SOC and only monopole (no exchange) interaction between the core and valence states [19, 29]. The second term is an *ad hoc* approximation based on the smallness of \mathbf{m} . Expressing the con-

ductivity tensor in terms of several fundamental spectral functions follows the spirit of Refs. [25, 30–33], and we show that it has to particularly simple form (1) in case of rutile antiferromagnets.

II. RESULTS

In Fig. 2, we demonstrate that our calculations accurately capture well the experimental x-ray absorption spectra (XAS) of NiF_2 , which are dominated by atomic multiplet features. Note that we use a single value for the lifetime broadening, which somewhat exaggerates the sharpness of the L_2 features.

The orientation and size of the Néel vector \mathbf{L} and magnetization \mathbf{m} vectors is determined by the external field \mathbf{B} , the inter-atomic exchange J_i and the single-ion anisotropy (SIA). We treat the inter-atomic exchange on the mean-field level while SIA appears through solution of the atomic problem with SOC and crystal-field. We begin our presentation with $\mathbf{B} \parallel [100]$. In this configuration, as reported in Ref. 35, a field of 0.7 T is sufficient to select the [100] domain (out of the four possible \mathbf{L} orientations). Increasing the magnetic field leads to a growth of $|\mathbf{m}|$. In Fig. 3(a) we present the XMCD spectra for $\hat{\mathbf{k}}$ along the applied field. The Hall vector points along [100] direction and has an amplitude $h(\omega) = \Delta_{\text{ALT}}(\omega) + \Delta_{\text{FM}}(\omega)|\mathbf{m}|$. In the absence of an external field, the calculated net magnetization is $\mathbf{m} = \mathbf{m}_s + \mathbf{m}_l = (0.023 + 0.027) \mu_B$, which somewhat overestimates the $0.03 \mu_B$ reported in literature [28, 36]. Calculations with reduced SOC, which reproduce the experimental value of magnetization can be found in the Supplementary Figures 4 and 5 [34]. The XMCD spectra calculated for various applied fields allow us to extract $\Delta_{\text{ALT}}(\omega)$ and $\Delta_{\text{FM}}(\omega)$, as shown in Fig. 3(c). The $\Delta_{\text{ALT}}(\omega)$ closely resembles the corresponding density obtained without valence SOC, a limit in which one can distinguish an altermagnet using non-relativistic symmetry. The validity of Eq. 1 is confirmed in Fig. 3(a,b). Fields up to 10 T result in more than a twofold increase of $|\mathbf{m}|$, providing sufficient variation of the XMCD spectra to facilitate a similar analysis of typical experimental data.

Next, we rotate the applied field, $\mathbf{B} = B(\cos \varphi_B, \sin \varphi_B, 0)$, in the (001) plane, as illustrated in Fig. 1(b). The calculated orientations of \mathbf{L} and \mathbf{m} , along with the magnitude $|\mathbf{m}|$, are shown in Fig. 4. These results align well with previous theoretical and experimental studies [28, 36]. The magnetic order arises from a competition between SIA, which favors the [010] and [100] orientations of \mathbf{L} and \mathbf{m} , respectively, and the external field, which \mathbf{L} and \mathbf{m} being perpendicular, with $\mathbf{m} \parallel \mathbf{B}$. At low field strengths, the orientations of the magnetic moments are only slightly perturbed. In the highest studied field of 40 T, the net magnetization \mathbf{m} follows the rotation of \mathbf{B} , though it remains misaligned, while the orthogonality of \mathbf{m} and \mathbf{L}

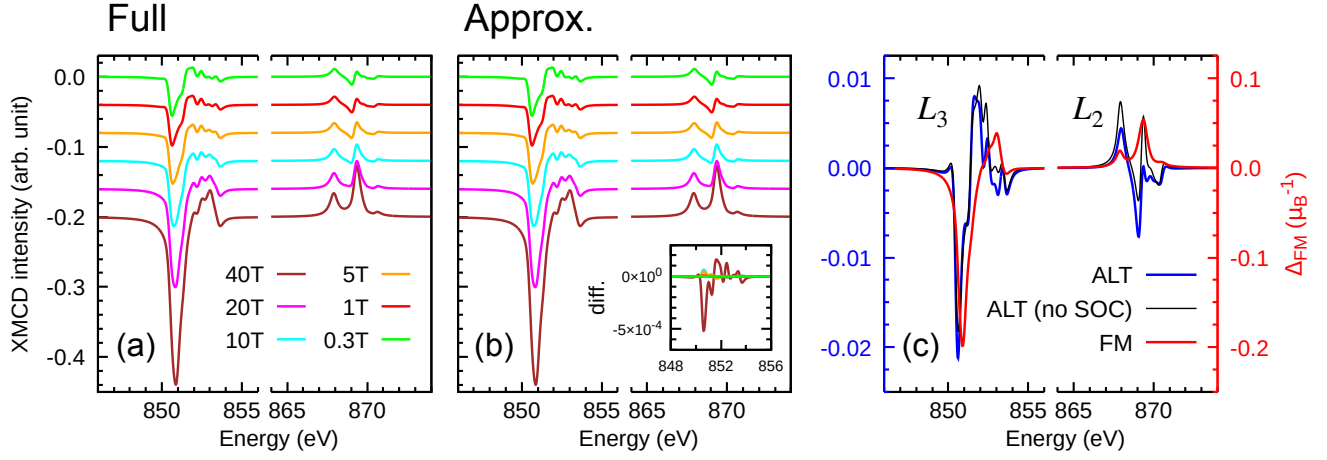


FIG. 3. (a) Ni $L_{2,3}$ -edge XMCD intensities in NiF_2 calculated independently for each magnetic field B and $\varphi_B = 0^\circ$ with no approximations to the method ('Full'). (b) XMCD intensities computed as a linear combination ('Approx.') of (c) $\Delta_{\text{ALT}}(\omega)$ (blue, left axis) and $\Delta_{\text{FM}}(\omega)$ (red, right axis) following Eq. 1. $\Delta_{\text{ALT}}(\omega)$ in the non-relativistic limit, calculated without the Ni $3d$ valence SOC, is also shown (thin black, left axis). The inset in panel (b) shows the difference in the XMCD intensities at the Ni L_3 -edge between the full calculations in (a) and the approximations in (b).

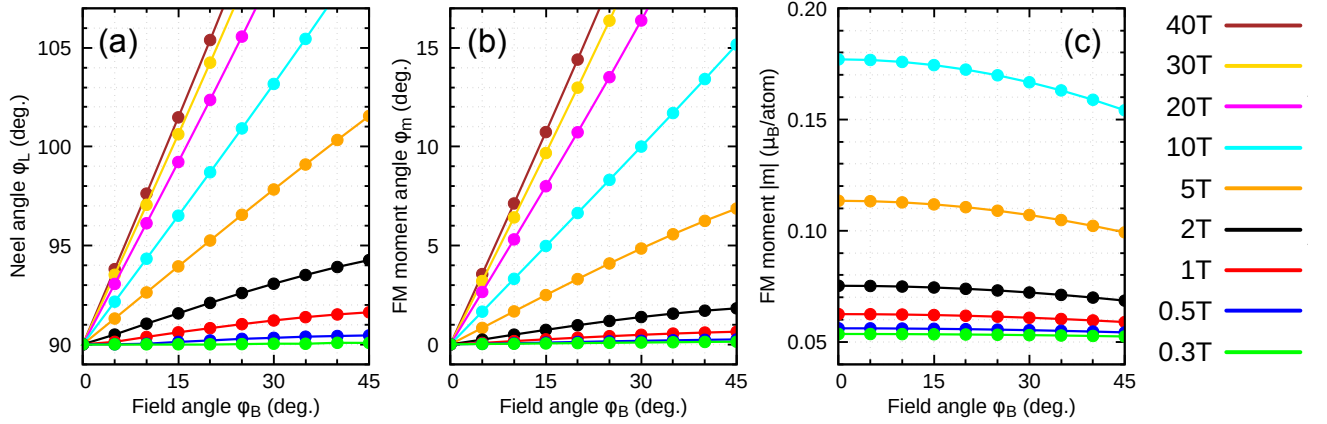


FIG. 4. Calculated relation between the angles of the external field φ_B and (a) the Néel vector φ_L , (b) the FM moment φ_m , and (c) the amplitude of the FM moment $|\mathbf{m}(\mathbf{B})|$ for selected amplitudes of the external field \mathbf{B} . The results over a wider range for the angles and amplitudes are provided in Supplementary Figure 4 [34].

is approximately maintained, reflecting the rigidity of Ni moments.

In Fig. 5 we show the field dependence of the XMCD spectra for the incoming light directions $[100]$ and $[010]$. A key observation is the comparison of the full calculation, which accounts for specific orientations of the Ni moments, and the spectra derived using Eq. 1 with the previously obtained spectral distributions $\Delta_{\text{ALT}}(\omega)$ and $\Delta_{\text{FM}}(\omega)$. We find that for all studied field strengths, up to 40 T, and across all field angles φ_B , Eq. 1 describes the calculated spectra with a relative accuracy better than 1%.

Finally, we present the data in a form that is closely aligned with a potential experimental setup. In this configuration, the external field \mathbf{B} is parallel to the light

beam $\hat{\mathbf{k}}$, and the sample is rotated along the c -axis, which is perpendicular to the beam. For $B = 0$ the Néel and magnetization vectors rotate with the sample, resulting in a $\cos \varphi_B$ dependence of the spectra. For a finite field the XMCD spectrum is described by Eq. 1 as

$$F_{\text{XMCD}}(\omega) = 2\Delta_{\text{ALT}}(\omega) \sin(\varphi_L + \varphi_B) + 2\Delta_{\text{FM}}(\omega) |\mathbf{m}| \cos(\varphi_m - \varphi_B) \approx 2\Delta_{\text{ALT}}(\omega) \cos(1 + \alpha)\varphi_B + 2\Delta_{\text{FM}}(\omega) m_0 \cos(1 - \alpha)\varphi_B, \quad (2)$$

where φ_L , φ_m and $|\mathbf{m}|$ depend on φ_B and the field amplitude, as illustrated in Fig. 4. Using the leading-order approximation $\varphi_L \simeq \varphi_m + \pi/2$, $|\mathbf{m}| \simeq m_0$ and $\varphi_m \simeq \alpha\varphi_B$, where α and m_0 depend on the field amplitude, we arrive

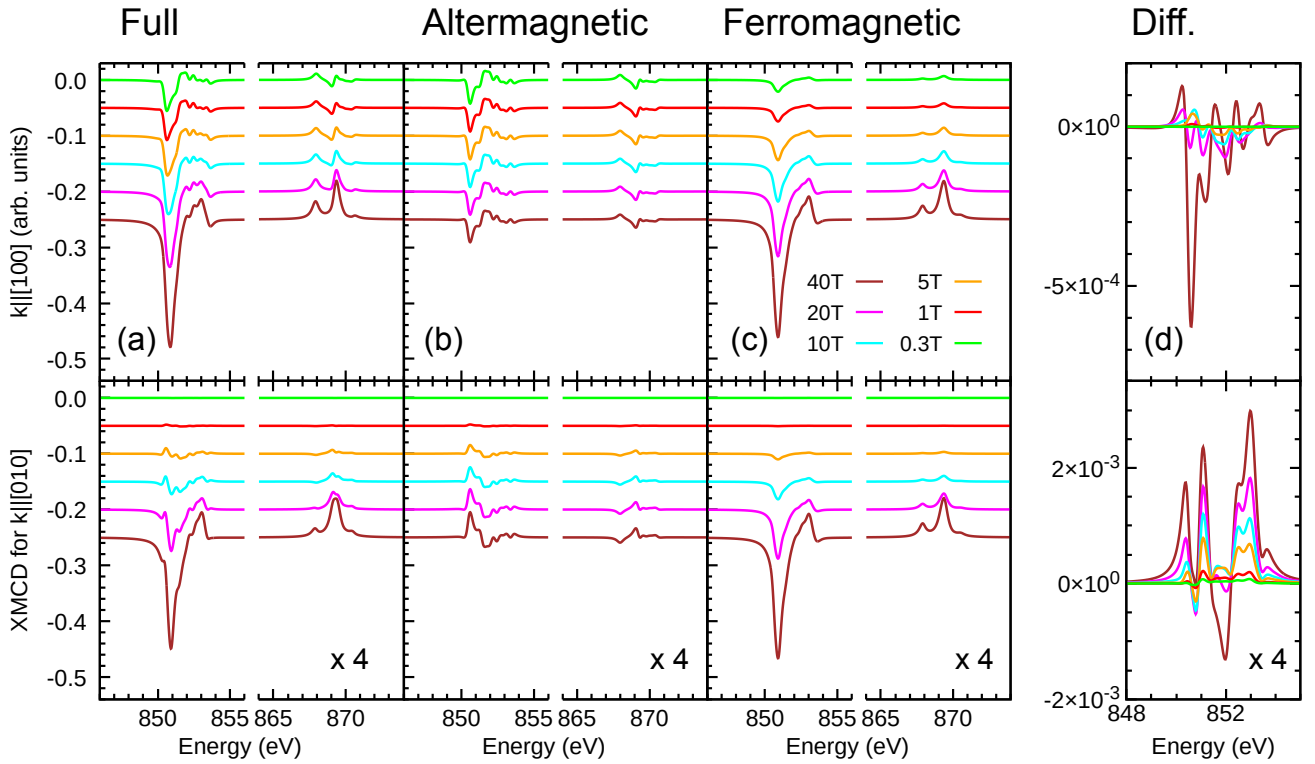


FIG. 5. (a) Ni $L_{2,3}$ -edge XMCD intensities in NiF_2 calculated for various amplitudes of the magnetic field B with $\varphi_B = 20^\circ$ for the two geometries of the light propagation vector $\hat{\mathbf{k}} = [100]$ (top) and $\hat{\mathbf{k}} = [010]$ (bottom). The altermagnetic contributions (b) and the ferromagnetic contributions (c) obtained from Eq. 1 using the magnetic order parameters shown in Fig. 4. (d) The difference between corresponding spectra in panel (a) and the sum of panels (b)+(c). The results for different angles φ_B can be found in Supplementary Figure 5 [34].

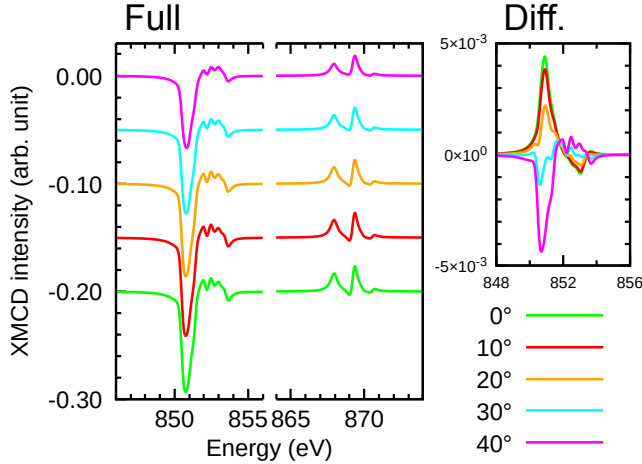


FIG. 6. (a) Ni $L_{2,3}$ -edge XMCD intensities in NiF_2 calculated with the magnetic field of 10 T and varying angles φ_B . The light propagation vector $\hat{\mathbf{k}} = \hat{\mathbf{B}}$ is used in the calculation. (b) The difference of the XMCD intensities between the full calculations in (a) and the approximations of Eq. 2 with $\alpha = 0.34$ and $m_0 = 0.17 \mu_B$.

at the bottom line. For sufficiently large fields ($\alpha \approx 0.34$ at 10 T) this dependence allows for experimental verification of the relationship $\hat{\mathbf{h}}_{\text{ALT}} = \mathcal{M}_{(110)} \hat{\mathbf{L}}(\mathbf{B})$ between the in-plane orientation of the Néel vector \mathbf{L} and the direction of the altermagnetic part of the Hall vector $\hat{\mathbf{h}}_{\text{ALT}}$ in the x-ray range. The results of a simulation for a field of 10 T are shown in Fig. 6.

Finally, we comment on the x-ray sum rules for orbital and spin moments [37] refer the reader to Supplementary Figure 6 [34] for quantitative analysis. There is no fundamental reason why the sum rules [37] should not apply to altermagnets the same way they apply to ferromagnets. However, given the small magnitude of the net moments and the oscillatory nature of the spectra, their application requires careful consideration. The present Full calculations fulfill the sum rules by design. The approximate formula of Eq. 1 fulfills the spin sum rule with 15% deviation over the studied parameter range, while deviation for orbital sum rules are as large as 30%. That Eq. 1 cannot capture the sum rules accurately is apparent from its form, implying that the effective moments obtained from sum rules scale with \mathbf{m} . The actual spin \mathbf{m}_s and orbital \mathbf{m}_l are not collinear and their relative contribution to the net \mathbf{m} strongly varies from approximately

1:1 without field to 5:1 at 40 T, see Supplementary Figure 2 [34].

III. DISCUSSION

We have conducted numerical simulations of XMCD at the $L_{2,3}$ edge of Ni in the rutile altermagnet NiF_2 under an external magnetic field. Our results demonstrate that the XMCD signal across a wide range of field amplitudes and ab -plane orientations can be expressed as a linear combination of two distinct spectral functions. These functions represent the altermagnetic and ferromagnetic contributions. The coefficients of this linear combination depend on the orientations of the Néel \mathbf{L} and the magnetization \mathbf{m} vectors. The ferromagnetic contribution scales with the amplitude of the magnetization. Moreover, the two contributions exhibit different angular dependencies as the external field rotates away from the easy-axis direction. This distinction provides an opportunity for experimental verification of the peculiar relationship [29] between the x-ray Hall vector and the Néel vector in the rutile structure.

The utility of Eq. 1 lies in the observation that the shape of the XMCD spectra in rutile altermagnets is roughly independent of the Néel vector \mathbf{L} in-plane orientation and its dependence on the photon incidence vector \mathbf{k} allows to determine \mathbf{L} uniquely. This contrasts the XMCD behavior in MnTe where the XMCD amplitude strongly depends on \mathbf{L} and even vanishes for specific orientations [20].

X-ray magneto-optics offers a distinct approach to isolating altermagnetic effects, leveraging the specific influence of valence spin-orbit coupling (SOC) in lighter elements, such as $3d$ transition metals. The valence SOC modifies the magnetic ground state by inducing canted moments and non-collinearity, while also affecting the excitation energies and the transition matrix elements. These intertwined effects are often difficult to disentangle in transport measurements or visible-range magneto-optics. In x-ray magneto-optics, however, the dominance of core-level SOC in transition metal elements naturally

separates these influences. As a result, the role of valence SOC is largely confined to determining the orientation of magnetic moments, which can also be externally controlled. This separation enables the systematic identification of the valence SOC effects, distinguishing them from the altermagnetic contribution.

IV. METHODS

We perform a density functional theory (DFT) calculation for the experimental structure of NiF_2 [38] using the Wien2K package [39]. The crystal field within the Ni $3d$ shell is derived from the self-consistent DFT band structure using the Wannier90 and wien2wannier packages [40, 41], see the Supplementary Note 1 [34] for the computational details. Since NiF_2 is a large-gap Mott insulator, the Ni^{2+} atomic model adequately accounts for the Ni $L_{2,3}$ -edge XAS spectrum dominated by the intra-atomic multiplet effects as shown by the early studies by de Groot *et al.* [20, 42]. The atomic Hamiltonian spanning the space of $2p$ and $3d$ shells consisting of the $3d$ crystal field, $2p$ and $3d$ SOC, $3d-3d$ and $2p-3d$ Coulomb interaction, Weiss mean-field and the external magnetic field is diagonalized. Full optical conductivity tensor in the Ni $L_{2,3}$ range is calculated in dipolar approximation using the Fermi golden rule. The total conductivity is the sum of the contributions from the two Ni sublattices in the rutile structure.

The magnetic ground state is obtained with Weiss mean-field theory. The Weiss field acting on local spin (Zeeman field) is calculated with the Heisenberg exchange parameters $J = 1.47$ meV derived from the experiment [36]. Since the dipole-dipole interaction energy for the studied antiferromagnetic order is degenerate for the all orientations of the Néel vector \mathbf{L} in the ab -plane we neglect it in our considerations.

V. DATA AVAILABILITY

Data are available from https://github.com/HarikiAtsushi/Repository_2025_NiF2_XMCD.

-
- [1] L. Šmejkal, J. Sinova, and T. Jungwirth, Emerging Research Landscape of Altermagnetism, *Phys. Rev. X* **12**, 040501 (2022).
 - [2] L. Šmejkal, J. Sinova, and T. Jungwirth, Beyond Conventional Ferromagnetism and Antiferromagnetism: A Phase with Nonrelativistic Spin and Crystal Rotation Symmetry, *Phys. Rev. X* **12**, 031042 (2022).
 - [3] K.-H. Ahn, A. Hariki, K.-W. Lee, and J. Kuneš, Antiferromagnetism in RuO_2 as d -wave Pomeranchuk instability, *Phys. Rev. B* **99**, 184432 (2019).
 - [4] M. Naka, S. Hayami, H. Kusunose, Y. Yanagi, Y. Motome, and H. Seo, Spin current generation in organic antiferromagnets, *Nature Communications* **10**, 4305 (2019).
 - [5] S. Hayami, Y. Yanagi, and H. Kusunose, Momentum-Dependent Spin Splitting by Collinear Antiferromagnetic Ordering, *J. Phys. Soc. Jpn.* **88**, 123702 (2019).
 - [6] L. Šmejkal, R. González-Hernández, T. Jungwirth, and J. Sinova, Crystal time-reversal symmetry breaking and spontaneous Hall effect in collinear antiferromagnets, *Sci. Adv.* **6**, eaaz8809 (2020).
 - [7] L.-D. Yuan, Z. Wang, J.-W. Luo, E. I. Rashba, and A. Zunger, Giant momentum-dependent spin splitting in centrosymmetric low- Z antiferromagnets, *Phys. Rev. B* **102**, 014422 (2020).

- [8] L.-D. Yuan, Z. Wang, J.-W. Luo, and A. Zunger, Prediction of low-Z collinear and noncollinear antiferromagnetic compounds having momentum-dependent spin splitting even without spin-orbit coupling, *Phys. Rev. Mater.* **5**, 014409 (2021).
- [9] S. Hayami, Y. Yanagi, and H. Kusunose, Bottom-up design of spin-split and reshaped electronic band structures in antiferromagnets without spin-orbit coupling: Procedure on the basis of augmented multipoles, *Phys. Rev. B* **102**, 144441 (2020).
- [10] I. I. Mazin, K. Koepernik, M. D. Johannes, R. González-Hernández, and L. Šmejkal, Prediction of unconventional magnetism in doped FeSb₂, *Proc. Natl. Acad. Sci. U.S.A.* **118**, e2108924118 (2021).
- [11] P. Liu, J. Li, J. Han, X. Wan, and Q. Liu, Spin-Group Symmetry in Magnetic Materials with Negligible Spin-Orbit Coupling, *Phys. Rev. X* **12**, 021016 (2022).
- [12] J. Yang, Z.-X. Liu, and C. Fang, Symmetry invariants and classes of quasi-particles in magnetically ordered systems having weak spin-orbit coupling, *arXiv:2105.12738*.
- [13] L. Šmejkal, A. H. MacDonald, J. Sinova, S. Nakatsuji, and T. Jungwirth, Anomalous Hall antiferromagnets, *Nat. Rev. Mater.* **7**, 482 (2022).
- [14] K. Samanta, M. Ležaić, M. Merte, F. Freimuth, S. Blügel, and Y. Mokrousov, Crystal Hall and crystal magneto-optical effect in thin films of SrRuO₃, *J. Appl. Phys.* **127**, 213904 (2020).
- [15] M. Naka, S. Hayami, H. Kusunose, Y. Yanagi, Y. Motome, and H. Seo, Anomalous Hall effect in κ -type organic antiferromagnets, *Phys. Rev. B* **102**, 075112 (2020).
- [16] S. Hayami and H. Kusunose, Essential role of the anisotropic magnetic dipole in the anomalous Hall effect, *Phys. Rev. B* **103**, L180407 (2021).
- [17] R. D. Gonzalez Betancourt, J. Zubáč, R. Gonzalez-Hernandez, K. Geishendorf, Z. Šobáň, G. Springholz, K. Olejník, L. Šmejkal, J. Sinova, T. Jungwirth, S. T. B. Goennenwein, A. Thomas, H. Reichlová, J. Železný, and D. Kriegner, Spontaneous Anomalous Hall Effect Arising from an Unconventional Compensated Magnetic Phase in a Semiconductor, *Phys. Rev. Lett.* **130**, 036702 (2023).
- [18] M. Naka, Y. Motome, and H. Seo, Anomalous Hall effect in antiferromagnetic perovskites, *Phys. Rev. B* **106**, 195149 (2022).
- [19] A. Hariki, Y. Takahashi, and J. Kuneš, X-ray magnetic circular dichroism in RuO₂, *Phys. Rev. B* **109**, 094413 (2024).
- [20] A. Hariki, A. Dal Din, O. J. Amin, T. Yamaguchi, A. Badura, D. Kriegner, K. W. Edmonds, R. P. Campion, P. Wadley, D. Backes, L. S. I. Veiga, S. S. Dhesi, G. Springholz, L. Šmejkal, K. Výborný, T. Jungwirth, and J. Kuneš, X-ray Magnetic Circular Dichroism in Altermagnetic α -MnTe, *Phys. Rev. Lett.* **132**, 176701 (2024).
- [21] N. Sasabe, M. Mizumaki, T. Uozumi, and Y. Yamasaki, Ferroic Order for Anisotropic Magnetic Dipole Term in Collinear Antiferromagnets of $(t_{2g})^4$ System, *Phys. Rev. Lett.* **131**, 216501 (2023).
- [22] H. Watanabe, K. Shinohara, T. Nomoto, A. Togo, and R. Arita, Symmetry analysis with spin crystallographic groups: Disentangling effects free of spin-orbit coupling in emergent electromagnetism, *Phys. Rev. B* **109**, 094438 (2024).
- [23] Z. Feng, X. Zhou, L. Šmejkal, L. Wu, Z. Zhu, H. Guo, R. González-Hernández, X. Wang, H. Yan, P. Qin, X. Zhang, H. Wu, H. Chen, Z. Meng, L. Liu, Z. Xia, J. Sinova, T. Jungwirth, and Z. Liu, An anomalous Hall effect in altermagnetic ruthenium dioxide, *Nat. Electron.* **5**, 735 (2022).
- [24] J. Jiménez-Mier, P. Olalde-Velasco, P. de la Mora, W. Yang, and J. D. Denlinger, Atomic multiplet and charge transfer effects in the resonant inelastic x-ray scattering (RIXS) spectra at the nickel L_{2,3} edge of NiF₂, *Journal of Nuclear Physics, Material Sciences, Radiation and Applications* **5**, 1 (2017).
- [25] J. Kuneš and P. M. Oppeneer, Anisotropic X-ray magnetic linear dichroism at the L_{2,3} edges of cubic Fe, Co, and Ni: *Ab initio* calculations and model theory, *Phys. Rev. B* **67**, 024431 (2003).
- [26] J. W. Stout and E. Catalano, Thermal anomalies associated with the antiferromagnetic ordering of FeF₂, CoF₂, and NiF₂, *Phys. Rev.* **92**, 1575 (1953).
- [27] R. A. Erickson, Neutron Diffraction Studies of Antiferromagnetism in Manganous Fluoride and Some Isomorphous Compounds, *Phys. Rev.* **90**, 779 (1953).
- [28] L. M. Matarrese and J. W. Stout, Magnetic anisotropy of NiF₂, *Phys. Rev.* **94**, 1792 (1954).
- [29] A. Hariki, T. Okauchi, Y. Takahashi, and J. Kuneš, Determination of the Néel vector in rutile altermagnets through x-ray magnetic circular dichroism: The case of MnF₂, *Phys. Rev. B* **110**, L100402 (2024).
- [30] N. Stojić, N. Binggeli, and M. Altarelli, Mn L_{2,3} edge resonant x-ray scattering in manganites: Influence of the magnetic state, *Phys. Rev. B* **72**, 104108 (2005).
- [31] E. Arenholz, G. van der Laan, R. V. Chopdekar, and Y. Suzuki, Anisotropic x-ray magnetic linear dichroism at the Fe L_{2,3} edges in Fe₃O₄, *Phys. Rev. B* **74**, 094407 (2006).
- [32] E. Arenholz, G. van der Laan, R. V. Chopdekar, and Y. Suzuki, Angle-dependent Ni²⁺ x-ray magnetic linear dichroism: Interfacial coupling revisited, *Phys. Rev. Lett.* **98**, 197201 (2007).
- [33] M. W. Haverkort, N. Hollmann, I. P. Krug, and A. Tanaka, Symmetry analysis of magneto-optical effects: The case of x-ray diffraction and x-ray absorption at the transition metal L_{2,3} edge, *Phys. Rev. B* **82**, 094403 (2010).
- [34] See Supplementary Material for details at ...
- [35] A. S. Borovik-Romanov, A. N. Bazhan, and N. M. Kreines, The weak ferromagnetism of NiF₂, *Zh. Eksp. Teor. Fiz.* **64**, 1367 (1973).
- [36] T. Moriya, Theory of magnetism of NiF₂, *Phys. Rev.* **117**, 635 (1960).
- [37] B. T. Thole, P. Carra, F. Sette, and G. van der Laan, X-ray circular dichroism as a probe of orbital magnetization, *Phys. Rev. Lett.* **68**, 1943 (1992).
- [38] J. W. Stout and S. A. Reed, The crystal structure of MnF₂, FeF₂, CoF₂, NiF₂ and ZnF₂, *Journal of the American Chemical Society* **76**, 5279 (1954).
- [39] P. Blaha, K. Schwarz, G. Madsen, D. Kvasnicka, and J. Luitz, *WIEN2k, An Augmented Plane Wave + Local Orbitals Program for Calculating Crystal Properties (Karlheinz Schwarz, Techn. Universität Wien, Austria, 2001), ISBN 3-9501031-1-2*.
- [40] A. A. Mostofi, J. R. Yates, G. Pizzi, Y.-S. Lee, I. Souza, D. Vanderbilt, and N. Marzari, An updated version of wannier90: A tool for obtaining maximally-localised

Wannier functions, Comput. Phys. Commun. **185**, 2309 (2014).

- [41] J. Kuneš, R. Arita, P. Wissgott, A. Toschi, H. Ikeda, and K. Held, Wien2wannier: From linearized augmented plane waves to maximally localized Wannier functions, Comput. Phys. Commun. **181**, 1888 (2010).
- [42] F. M. F. de Groot, J. C. Fuggle, B. T. Thole, and G. A. Sawatzky, *2p* X-ray absorption of *3d* transition-metal compounds: An atomic multiplet description including the crystal field, Phys. Rev. B **42**, 5459 (1990).

ACKNOWLEDGMENTS

We thank Karel Výborný, Jakub Železný and Anna Kauch for discussions and critical reading of the

manuscript. This work was supported by JSPS KAKENHI Grant Numbers 21K13884, 21H01003, 23K03324, 23H03817 (A.H.), and by the project Quantum materials for applications in sustainable technologies (QM4ST), funded as project No. CZ.02.01.01/00/22_008/0004572 by Programme Johannes Amos Comenius, call Excellent Research and by the Ministry of Education, Youth and Sports of the Czech Republic through the e-INFRA CZ (ID:90254). Part of the computations in this work were performed using the facilities of the Supercomputer Center, the Institute for Solid State Physics, the University of Tokyo.

Supplementary Material to “Separating Antiferromagnetic and Ferromagnetic Effects in X-ray Magnetic Dichroism of Rutile NiF_2 ”

A. Hariki,¹ K. Sakurai,¹ T. Okauchi,¹ and J. Kuneš²

¹*Department of Physics and Electronics, Graduate School of Engineering,
Osaka Metropolitan University, 1-1 Gakuen-cho, Nakaku, Sakai, Osaka 599-8531, Japan*

²*Department of Condensed Matter Physics, Faculty of Science,
Masaryk University, Kotlářská 2, 611 37 Brno, Czechia*

Supplementary Note 1 Mean-field calculation and XMCD simulation

Ni L -edge x-ray magnetic circular dichroism (XMCD) spectra were calculated based on the Ni^{2+} atomic model with the Weiss field \mathbf{b} in the magnetically ordered state, as determined within a mean-field calculation for the spin exchange interaction. First, density functional theory (DFT) calculations were performed using the WIEN2K package [1] within the local density approximation for the exchange-correlation potential. The experimental rutile structure [2] was employed in the DFT calculations. The crystal-field term, h^{CF} , in the atomic model Hamiltonian was derived from the DFT band structure by projecting the Ni $3d$ bands near the Fermi level onto a tight-binding model using the wannier90 and wien2wannier packages [3, 4]. The h^{CF} term is expressed in the crystal-field basis $(x'y', 3z'^2 - r'^2, x'^2 - y'^2, z'x', y'z')$ with respect to the local coordinate system $(x'y'z')$ shown in Fig. S1 as,

$$h^{\text{CF}} = \begin{pmatrix} -0.107 & 0 & 0 & 0 & 0 \\ 0 & -0.141 & -0.043 & 0 & 0 \\ 0 & -0.043 & -1.058 & 0 & 0 \\ 0 & 0 & 0 & -0.954 & 0 \\ 0 & 0 & 0 & 0 & -0.828 \end{pmatrix}.$$

The d - d interaction within the Ni^{2+} configuration can be parameterized by the Hubbard $U = F_0$ and Hund's coupling $J_{\text{H}} = (F_2^{dd} + F_4^{dd})/14$. In the atomic model with a fixed number of Ni $3d$ electrons ($3d^8$), the monopole term F_0 contributes only to an overall energy shift and is therefore irrelevant to our analysis. The Hund's coupling parameter is set to $J_{\text{H}} = 0.86$ eV, a typical value for Ni^{2+} systems.

To simulate the magnetically ordered state, we take into account the antiferromagnetic exchange interaction between nearest-neighbor Ni spins of $S = 1$ based on the spin Heisenberg Hamiltonian $\mathcal{H} = J \sum_{\langle i,j \rangle} \mathbf{S}_i \cdot \mathbf{S}_j$ with $J = 1.47$ meV [5]. The exchange interaction is treated within a static mean-field approximation. In the self-consistent loop for determining the Weiss field \mathbf{b} , which represents the effective field from surrounding spins, the local spin expectation values $\langle \mathbf{S} \rangle$ are computed from the Ni^{2+} atomic model described above, explicitly incorporating all 45 multiplet states in the $3d^8$ configuration. When an external field \mathbf{B} is applied, it acts on both the Ni spin (\mathbf{m}_s) and the orbital (\mathbf{m}_l) magnetic moments at the Ni sites. The spin-orbit coupling (SOC) on the Ni $3d$ shell is included in the mean-field calculation, as well as in the XMCD simulations described below. The SOC constants, $\xi = 77$ meV and

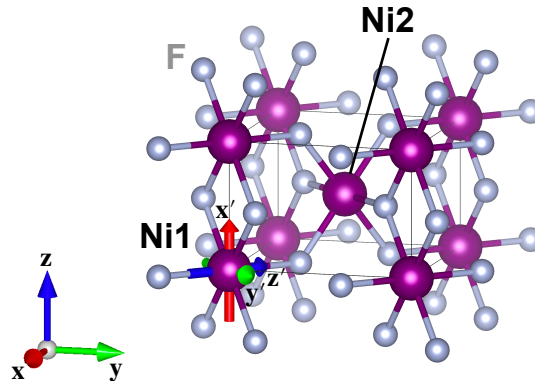


FIG. S1. The crystal structure of NiF_2 and a local coordinate $(x'y'z')$.

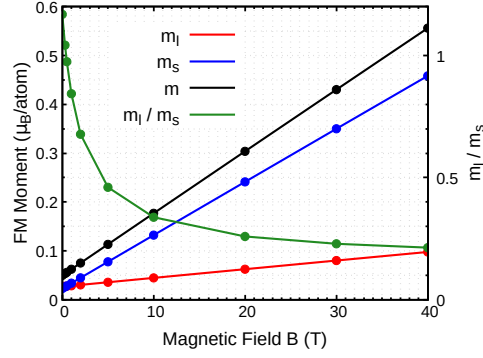


FIG. S2. Total (m), orbital (m_l), and spin (m_s) components of the ferromagnetic moment, calculated independently for each magnetic field \mathbf{B} at $\varphi_B = 0^\circ$. The ratio m_l/m_s is shown on the right vertical axis.

83 meV, were obtained from the DFT calculation and atomic Hartree-Fock calculations [6, 7], respectively. Table I summarizes the Ni ferromagnetic components and the corresponding Weiss field \mathbf{b} in the absence of the external field \mathbf{B} for a wide range of SOC values. In the solutions in Table I, the antiferromagnetic Néel vector \mathbf{L} is aligned along the [010] direction ($\varphi_L = 90^\circ$). To account for hybridization effects with ligands, as explained below, the SOC value was reduced to $\xi = 50$ meV in the presented results. With $\xi = 50$ meV, the calculated magnetic moment is $m = 0.050 \mu_B$, which agrees reasonably well with previous estimates [5, 8]. In Ref. [5], a value of $\xi = 37$ meV was used. As discussed in Sec. III, our main conclusion regarding the XMCD properties remains unaffected by the specific choice of the SOC constant. Figure S2 shows the evolution of the magnetic moments computed with $\xi = 50$ meV under the external magnetic field \mathbf{B} applied along the [100] axis ($\varphi_B = 0^\circ$). As discussed in the main text, the orbital moment contribution is significant in the absence of the external field but is reduced with the field, as reflected in the ratio of m_l/m_s shown in Fig. S2.

ξ (meV)	100	83	77	50	37	35	30
m_s (μ_B)	0.087	0.061	0.053	0.023	0.013	0.012	0.009
m_l (μ_B)	0.063	0.050	0.045	0.027	0.020	0.018	0.016
m (μ_B)	0.150	0.111	0.098	0.050	0.033	0.030	0.025
$b_{[100]}$ (meV)	-0.257	-0.181	-0.155	-0.067	-0.038	-0.034	-0.025
$b_{[010]}$ (meV)	5.784	5.818	5.829	5.864	5.875	5.877	5.880

TABLE I. Total (m), orbital (m_l), and spin (m_s) contributions to the ferromagnetic moment (per Ni atom) along the [100] direction, calculated for different values of the SOC constant ξ . The Weiss field \mathbf{b} acting on the Ni1 site along the [100] and [010] directions is also shown.

	F_2^{dd}	F_4^{dd}	F_2^{pd}	G_1^{pd}	G_3^{pd}	ξ_{2p}
Values (eV)	7.409	4.631	6.563	4.919	2.797	11.507

TABLE II. Ni^{2+} atomic Slater integral values for the $3d$ - $3d$ (valence-valence) and $2p$ - $3d$ (core-valence) interactions, as well as the $2p$ core-orbital SOC ξ_{2p} values used in the Ni^{2+} atomic model. Here, F and G represent the direct and exchange integrals, respectively.

After obtaining the mean-field solution for the spin Heisenberg Hamiltonian \mathcal{H} , we compute the XMCD using the atomic model with the Weiss field \mathbf{b} from the converged solution. At this step, the Ni $2p$ core orbitals and their interaction with the Ni $3d$ electrons are considered explicitly. The Slater integrals for the $2p$ - $3d$ interaction ($F_2^{pd}, G_1^{pd}, G_3^{pd}$) and the $2p$ core-orbital SOC (ξ_{2p}) parameters were estimated using atomic Hartree-Fock calculations,

as described in Refs. [6, 7]. These parameter values are listed in Table II. The x-ray absorption spectroscopy (XAS) spectral function is expressed using Fermi's golden rule

$$F_{\text{XAS}}^{(i)}(\omega_{\text{in}}) = -\frac{1}{\pi} \text{Im} \langle g | T^\dagger \frac{1}{\omega_{\text{in}} + E_g - H_i} T | g \rangle.$$

Here, $|g\rangle$ represents the ground state with energy E_g , and ω_{in} denotes the energy of the incident photon. The operator T corresponds to the electric dipole transition operator for circularly-polarized x-rays. The index i ($i = 1, 2$) indicates the x-ray excited Ni site within the unit cell. The atomic Hamiltonian H_i for each Ni site is used to calculate its individual contribution to the spectra [9, 10]. The total XMCD intensities are then obtained by summing the contributions from the two sites.

Supplementary Note 2 NiF₆ cluster model simulation and spin-orbit coupling dependence

In Fig. S3, we compare the energy splittings of the lowest $S = 1$ states in the local excitation spectrum without both the external and exchange fields between the NiF₆ cluster model and the Ni²⁺ atomic model. These splittings reflect the single-ion anisotropy. The NiF₆ cluster model explicitly includes hybridization with ligands, whereas in the atomic model, this effect is incorporated into the d level energies effectively. The hybridization parameters in the NiF₆ cluster model, summarized in Table II, were derived from a tight-binding model Hamiltonian that explicitly includes both the Ni $3d$ and F $2p$ DFT bands (see Ref. [11] for details about our construction of the cluster model). The averaged Coulomb interaction U_{dd} and charge-transfer energy Δ_{CT} in the cluster-model Hamiltonian were adopted from Ref. [12]. The cluster model implements $\xi = 83$ meV, obtained from atomic Hartree-Fock calculations. The Ni²⁺ atomic model with $\xi = 50$ meV reproduces a similar splitting, Δ_1 , between the lowest and first excited states as obtained in the NiF₆ cluster model calculations. Thus, we used the reduced value $\xi = 50$ meV in our atomic model calculations in the main text to account for ligand hybridization effects.

	U_{dd}	Δ_{CT}	$V_{B_{1g}}$	V_{A_g}	$V_{A'_g}$	$V_{B_{2g}}$	$V_{B_{3g}}$
Values (eV)	6.50	4.30	2.18	2.06	1.19	1.18	1.06

TABLE III. The parameter values for configuration-averaged $3d-3d$ Coulomb interaction (U_{dd}), charge-transfer energy (Δ_{CT}) and the metal-ligand hybridization amplitude adopted in the NiF₆ cluster model in eV unit. U_{dd} and Δ_{CT} are taken from Ref. [12].

$ \text{Ex2}\rangle$	$\updownarrow \Delta_2$		NiF ₆ cluster ($\xi=83\text{meV}$)	Atomic model ($\xi=83\text{meV}$)	Atomic model ($\xi=50\text{meV}$)	Atomic model ($\xi=37\text{meV}$)
$ \text{Ex1}\rangle$	$\updownarrow \Delta_1$	Δ_1 (meV)	0.54	1.33	0.51	0.29
$ \text{GS}\rangle$		Δ_2 (meV)	0.36	0.23	0.08	0.04

FIG. S3. The energy splittings between the ground state and the first excited state (Δ_1), as well as between the first and second excited states (Δ_2) within the lowest $S = 1$ states, are shown for the NiF₆ cluster model and the atomic model in meV unit. For the atomic model, simulations were conducted with three different SOC constants ξ (83 meV, 50 meV, 37 meV).

Supplementary Note 3 Dependence of the Magnetic State and XMCD on SOC

Figure S4 summarizes the magnetic state and XMCD properties for different Ni $3d$ SOC values, $\xi = 50$ meV and $\xi = 37$ meV, respectively. The magnetic moments in the absence of an external field are listed in Table I. The smaller SOC value, $\xi = 37$ meV, appears to yield magnetic moment values close to existing experimental estimates [5, 8]. As expected for weaker SOC, the ferromagnetic moment is reduced, while the tilt of the Néel vector \mathbf{L} induced by an external field with $\varphi_B \neq 0$ is enhanced slightly compared to the case with $\xi = 50$ meV. We found that the Ni L -edge XMCD properties are very similar for the two SOC values. In particular, the approximation for the XMCD intensities

based on Eq. (1) provides comparable accuracy in both cases, as shown in Fig. S4(e). We provide the XMCD data for various φ_B values in Fig. S5.

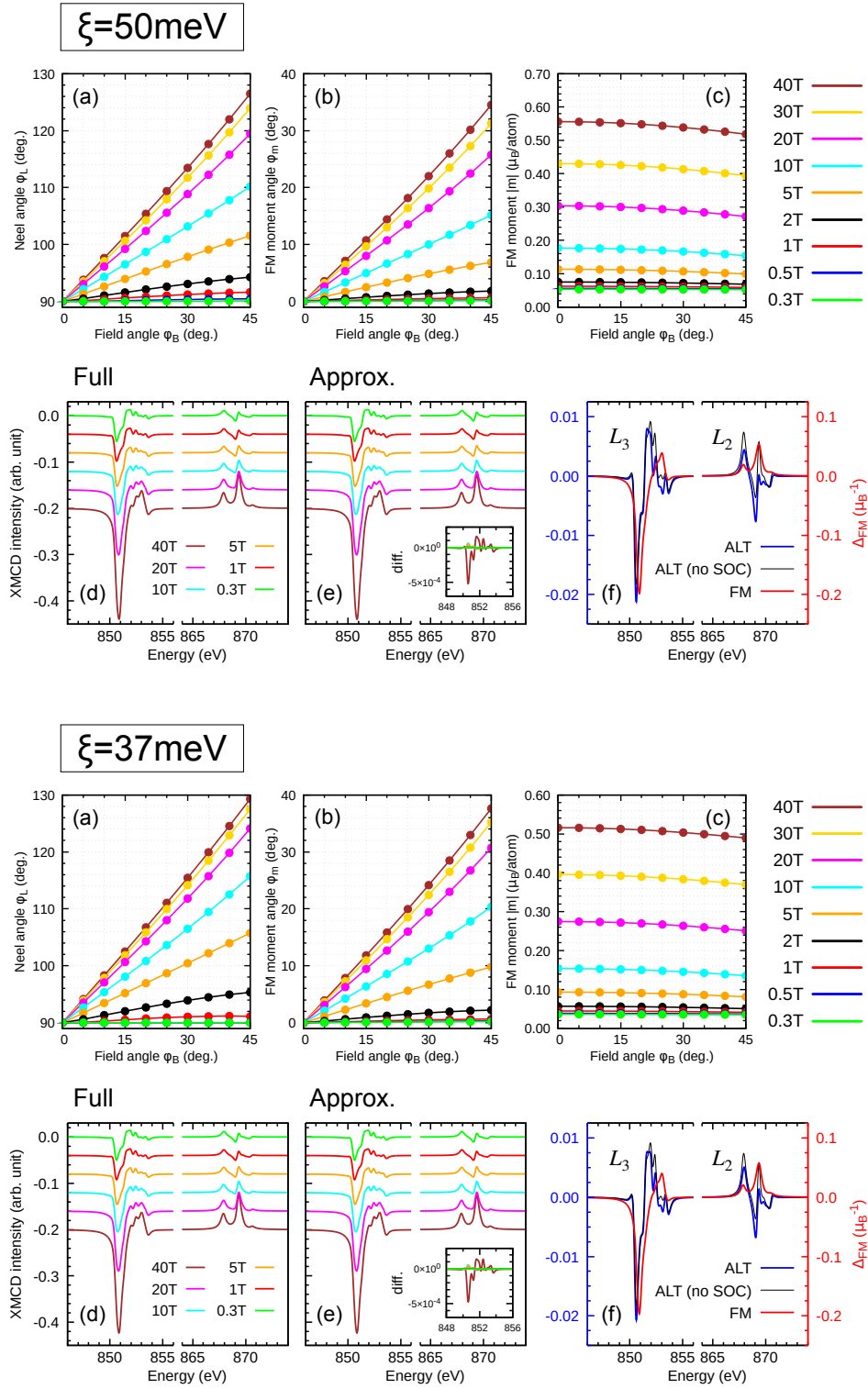


FIG. S4. Calculated relation (with $\xi = 50$ meV and 37 meV) between the angles of the external field φ_B and (a) the Néel vector φ_L , (b) the FM moment φ_m , and (c) the amplitude of the FM moment $|\mathbf{m}(\mathbf{B})|$ for selected amplitudes of the external field \mathbf{B} . (d) Ni $L_{2,3}$ -edge XMCD intensities in NiF_2 calculated independently for each magnetic field B and $\varphi_B = 0^\circ$ with no approximations to the method ('FULL'). (e) XMCD intensities computed as a linear combination ('APPROX.') of (f) $\Delta_{\text{ALT}}(\omega)$ (blue, left axis) and $\Delta_{\text{FM}}(\omega)$ (red, right axis). $\Delta_{\text{ALT}}(\omega)$ in the nonrelativistic limit, calculated without the Ni 3d valence SOC, is also shown (thin black, left axis). The inset in panel (e) shows the difference in the XMCD intensities at the Ni L_3 -edge between the full calculations in (d) and the approximations in (e).

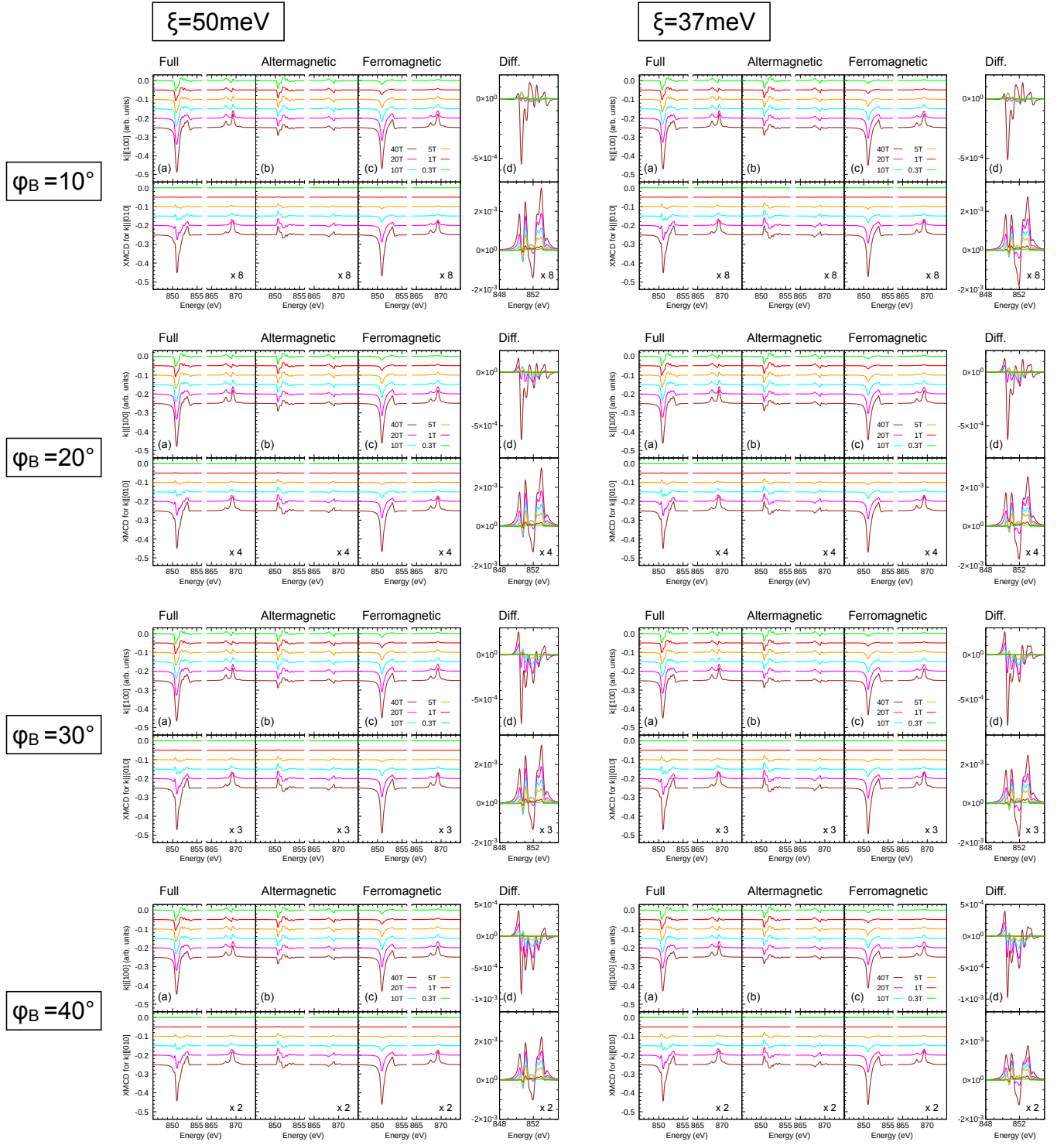


FIG. S5. (a) Ni $L_{2,3}$ -edge XMCD intensities in NiF_2 calculated for various magnetic field amplitudes B with $\varphi_B = 10^\circ, 20^\circ, 30^\circ$, and 40° (from top to bottom) for the two geometries of the light propagation vector $\hat{\mathbf{k}} = [100]$ (top) and $\hat{\mathbf{k}} = [010]$ (bottom). The left and right panels show results obtained with $\xi = 50$ meV and $\xi = 37$ meV, respectively. (b) Altermagnetic contributions. (c) Ferromagnetic contributions. (d) The difference in XMCD intensities at the Ni L_3 -edge between the full calculations in (a) and the approximations using Eq. (1) in the main text.

Supplementary Note 4 Analysis of the XMCD sum rule

Figure 6 summarizes the orbital moment \mathbf{L} and effective spin $\mathbf{S}_{\text{eff}} = \mathbf{S} + \frac{7}{2}\mathbf{T}$ derived from the sum rule applied to the simulated XMCD results. The exact values correspond to those obtained from the sum rule for the “Full” spectra in the main text. We checked numerically that these values are consistent with the expectation values directly evaluated from the atomic-model ground state. The values derived from the approximated XMCD based on Eq. (1) are compared with the exact values. The approximated values accurately reproduce the exact ones in the weak external field \mathbf{B} , while the error increases somewhat as the field strength increases. For 40 T, deviation of 14.6 % and 9.11 % at $\varphi_B = 0^\circ$ is expected for the orbital and effective spin values, respectively. When the field is rotated to $\varphi_B = 20^\circ$, the deviation for the [100] component remains nearly unchanged (14.4 % for \mathbf{L} , 9.16 % for \mathbf{S}_{eff}). However, for the [010] component, particularly for \mathbf{L} , it increases (36.1 % for \mathbf{L} , 11.7 % for \mathbf{S}_{eff}).

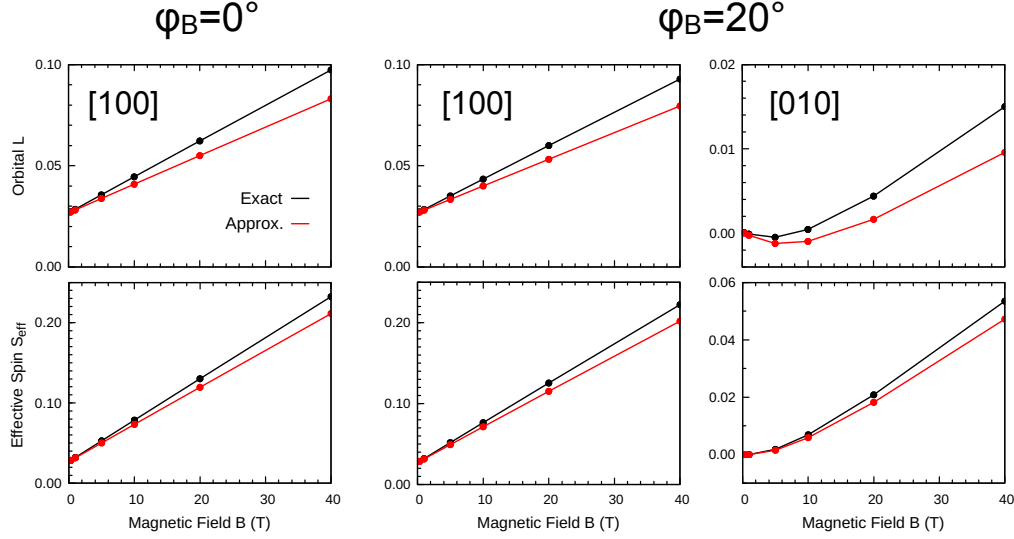


FIG. S6. The orbital angular momentum L (top) and effective spin $S_{\text{eff}} = S + \frac{7}{2}T$ (bottom) obtained from the exact XMCD simulation (black) and the approximate scheme in Eq. (1) (red) are shown for $\varphi_B = 0^\circ$ (left) and $\varphi_B = 20^\circ$ (middle, right) and different amplitudes of the external field \mathbf{B} . The middle and right panels correspond to the projections of these quantities onto the [100] and [010] directions, respectively.

-
- [1] P. Blaha, K. Schwarz, G. Madsen, D. Kvasnicka, and J. Luitz, *WIEN2k, An Augmented Plane Wave + Local Orbitals Program for Calculating Crystal Properties* (Karlheinz Schwarz, Techn. Universitat Wien, Austria, 2001), ISBN 3-9501031-1-2.
 - [2] J. W. Stout and S. A. Reed, *Journal of the American Chemical Society* **76**, 5279 (1954).
 - [3] A. A. Mostofi, J. R. Yates, G. Pizzi, Y.-S. Lee, I. Souza, D. Vanderbilt, and N. Marzari, *Comput. Phys. Commun.* **185**, 2309 (2014).
 - [4] J. Kuneš, R. Arita, P. Wissgott, A. Toschi, H. Ikeda, and K. Held, *Comput. Phys. Commun.* **181**, 1888 (2010).
 - [5] T. Moriya, *Phys. Rev.* **117**, 635 (1960).
 - [6] A. Hariki, T. Uozumi, and J. Kuneš, *Phys. Rev. B* **96**, 045111 (2017).
 - [7] A. Hariki, M. Winder, T. Uozumi, and J. Kuneš, *Phys. Rev. B* **101**, 115130 (2020).
 - [8] L. M. Matarrese and J. W. Stout, *Phys. Rev.* **94**, 1792 (1954).
 - [9] A. Hariki, Y. Takahashi, and J. Kuneš, *Phys. Rev. B* **109**, 094413 (2024).
 - [10] M. Winder, A. Hariki, and J. Kuneš, *Phys. Rev. B* **102**, 085155 (2020).
 - [11] T. Yamaguchi, K. Higashi, A. Regoutz, Y. Takahashi, M. Lazemi, Q. Che, F. M. F. de Groot, and A. Hariki, *Phys. Rev. B* **109**, 205143 (2024).
 - [12] K. Okada and A. Kotani, *J. Phys. Soc. Japan* **60**, 772 (1991).